Atmospheric Research 99 (2011) 263–276

Contents lists available at ScienceDirect

Atmospheric Research

journal homepage: www.elsevier.com/locate/atmos

Aerosol properties and associated radiative effects over Cairo (Egypt)

M. El-Metwally [a,*], S.C. Alfaro [b], M.M. Abdel Wahab [c], O. Favez [d], Z. Mohamed [a], B. Chatenet [b]

[a] Physics Department, Faculty of Science, Port Said University, Port Said, Egypt
[b] LISA-UMR CNRS 7583, Universités de Paris 12 et de Paris 7, Créteil, France
[c] Astronomy and Meteorology Department, Faculty of Science, Cairo University, Giza, Egypt
[d] LSCE/IPSL, Laboratoire CEA-CNRS-UVSQ, CEA Orme des Merisiers, 91191 Gif-sur-Yvette, France

ARTICLE INFO

Article history:
Received 26 December 2009
Received in revised form 12 October 2010
Accepted 13 October 2010

Keywords:
Aerosol radiative forcing
Forcing efficiency
Aerosol optical depth
Aerosol size distribution
Heating rate
CACHE
AERONET
Cairo

ABSTRACT

Cairo is one of the largest megacities in the World and the particle load of its atmosphere is known to be particularly important. In this work we aim at assessing the temporal variability of the aerosol's characteristics and the magnitude of its impacts on the transfer of solar radiation. For this we use the level 2 quality assured products obtained by inversion of the instantaneous AERONET sunphotometer measurements performed in Cairo during the Cairo Aerosol CHaracterization Experiment (CACHE), which lasted from the end of October 2004 to the end of March 2006. The analysis of the temporal variation of the aerosol's optical depth (AOD) and spectral dependence suggests that the aerosol is generally a mixture of at least 3 main components differing in composition and size. This is confirmed by the detailed analysis of the monthly-averaged size distributions and associated optical properties (single scattering albedo and asymmetry parameter). The components of the aerosol are found to be 1) a highly absorbing background aerosol produced by daily activities (traffic, industry), 2) an additional, 'pollution' component produced by the burning of agricultural wastes in the Nile delta, and 3) a coarse desert dust component. In July, an enhancement of the accumulation mode is observed due to the atmospheric stability favoring its building up and possibly to secondary aerosols being produced by active photochemistry. More generally, the time variability of the aerosol's characteristics is due to the combined effects of meteorological factors and seasonal production processes.

Because of the large values of the AOD achieved during the desert dust and biomass burning episodes, the instantaneous aerosol radiative forcing (RF) at both the top (TOA) and bottom (BOA) of the atmosphere is maximal during these events. For instance, during the desert dust storm of April 8, 2005 RF_{BOA}, RF_{TOA}, and the corresponding atmospheric heating rate peaked at −161.7 W/m^2, −65.8 W/m^2, and 4.0 K/d, respectively. Outside these extreme events, the distributions of the radiative forcing values at BOA and TOA are Gaussian with means and standard deviations of −58 (±27), and −19(±11)W/m^2, respectively. These two negative values indicate a cooling effect at the 2 atmospheric levels but the largest absolute value at BOA corresponds to a trapping of solar radiation inside the atmosphere. The averages of the instantaneous forcing efficiencies (FE) derived from measurements performed at solar zenith angles between 50 and 76° are −195 (±42) and −62(±17)W/m^2.AOD_{550} for BOA and TOA, respectively. The value at TOA is larger than in other urban environments, which could be due to the desert dust component backscattering more solar radiation to space than absorbing urban aerosols. The lower absorption of solar light by desert dust also explains qualitatively the lower than usual value of FE_{BOA}. A more precise study of the effects of the desert dust and biomass burning aerosols shows that fluctuations of their monthly-averaged concentrations explain the departures of the TOA and BOA radiative forcings from the background situation. In April, the contributions of DD to the month averages of the instantaneous radiative forcing are as high as 53% at BOA, and 66% at TOA. In October, the biomass burning mode contributes 33 and 27% of these forcings, respectively. Noteworthy is that

* Corresponding author.
E-mail address: melmetwally@yahoo.com (M. El-Metwally).

0169-8095/$ – see front matter
doi:10.1016/j.atmosres.2010.10.017

the contribution of DD to RF is never less than 17% (at BOA) and 27% (at TOA), emphasizing the importance of the mineral dust component on the transfer of solar radiation above Cairo, and this even in months when no major dust storm is observed.

1. Introduction

Several studies have demonstrated that both natural and anthropogenic aerosols have important effects on the climate of the Earth–atmosphere system (e.g., Haywood and Shine, 1997). Aerosol particles affect the climate directly by scattering and absorbing solar radiation and indirectly by favoring formation of clouds or by modifying their microphysical properties. However, as a consequence of their high spatial and temporal variability, these effects are strongly regional in magnitude and sign (Nakajima et al., 2003). Thus, the overall (annual, global) quantification of the impact of aerosols on the Earth's radiative balance is highly uncertain. This emphasizes the need for accurate data on aerosol and environmental properties and explains that multiple-measurement approaches have been designed to quantify more precisely the impacts of aerosols on climate, at least on a regional basis. These approaches seek to combine satellite observations, continued observations from ground networks, and data from dedicated field experiments (e.g., Kaufman et al., 2002).

Aerosol particles, among which desert dust, smoke from biomass burning, and urban–industrial pollution (Kaufman et al. 1997), can affect the radiation budget and the temperature field by changing the energy balance and distribution of solar and terrestrial radiation in the atmosphere. More precisely, the addition of aerosols to the atmosphere increases absorption of solar radiation and modifies the scattering of sunlight. The reflection of radiation to space may counteract the greenhouse warming by cooling the earth system (Charlson et al., 1992) and the redistribution of radiation is expected to change the temperature profiles (Alpert et al. 1998), the atmospheric stability and possibly cloud formation (Ackerman et al. 2000). At any given altitude of the atmosphere, the result of absorption and scattering is a modification of the vertical net flux of solar radiation. This perturbation of sunlight by aerosols is designated as the 'radiative forcing' (RF). The values of RF at the bottom (RF_{BOA}) and top (RF_{TOA}) of the atmosphere are key parameters in the quantification of the impact of aerosols on climate. However, the assessment of RF is a difficult task because it is characterized by a large spatial and temporal heterogeneity resulting itself from the wide variety of aerosol sources and types, the spatial non-uniformity and intermittency of these sources, the short atmospheric lifetime of aerosols, and the chemical and microphysical processes that occur in the atmosphere (Chin 2009).

With its newer generation of sensors, such as the Moderate Resolution Imaging Spectroradiometer (MODIS) implemented onboard NASA's Earth Observing System (e.g., King et al., 1992), satellite remote sensing is a promising tool for studying the distribution of aerosols and associated effects from global to local scales. However, satellite-retrieved properties are often uncertain because of necessary a priori assumptions, in particular over continents. Thus, networks of ground-based radiometers have been established to provide quality reference points. This is the case of the Aerosol Robotic Network (AERONET), a federated network of more than 200 automatic Sun/Sky radiometers worldwide (Holben et al., 1998), which has been established to measure aerosol optical thickness and other columnar aerosol properties. In areas such as the Mediterranean basin where significant aerosol loads of pollution, biomass burning and advected mineral dust have led to one of the largest regional TOA energy losses worldwide (e.g., Haywood and Boucher, 2000; Lelieveld et al., 2002; Andreae et al., 2002), the measurements by individual instruments can be particularly useful for the quantification of the regional impact of aerosols on the radiative energy balance. Provided a parallel individuation of aerosol types is possible, these local studies can also help reduce the uncertainties on the effect of individual aerosol species, which is necessary because according to the recent report of IPCC (2007) the direct radiative forcing by individual aerosol species is less certain than the total direct radiative forcing by all aerosols.

In this work we will use the measurements performed by the Cimel sunphotometer implemented in the city of Cairo for the duration of the Cairo Aerosol Characterization Experiment (CACHE), namely from the end of Oct. 2004 to the end of March 2006. This instrument was incorporated in the AERONET network and the inversion of its measurements allows assessment of 1) the seasonal variability of the overall radiative forcing, and 2) of the effects of individual aerosol species.

Practically, the paper is organized in two main parts: Section 2 provides a description of the local context, of the available database and of the methodology applied to invert the AERONET measurements, whereas Section 3 discusses the results in terms of variability of 1) aerosol properties and 2) impact on the radiative transfer of solar light at the top and bottom of the atmosphere.

2. Experimental site and methods

2.1. Site location and meteorological context

Cairo is located at the southernmost tip of the Nile delta, at the limit between lower and upper Egypt. With its 16 million inhabitants, Greater Cairo is one of the largest cities in the World and also one of the most polluted. This is a direct result of the growth in population and associated activities that have been observed during the last decades. Motorized traffic and industries located within the city itself or in the neighboring areas of Helwan (south of Cairo) and Shoubra El-Kheima (in the north) are particle sources active all year round but additional material produced by seasonal sources located outside the city can also be transported towards it at certain times of the year.

Meteorological factors also contribute to the seasonal variability of the aerosol loading. The general features of the

city's climate have been described by El-Wakil et al. (2001). All year round, prevailing winds are from the north but occasional chained depressions known as 'Khamsin' depressions in Arabic, and whose probability of occurrence is largest in spring, give birth to strong winds blowing from the south/southwest and raising large amounts of desert dust on their way. Though the air masses associated with these events are warm and relatively dry, occasional clouds, rainfall and thunderstorms may also be observed during these periods (El-Fandy, 1940). In summer and autumn the weakening of north winds combined with frequent temperature inversions at about 300–1000 masl (El-Fandy and El-Nisr, 1949; El-Wakil et al., 2001; Tadros et al., 2002; Zakey et al., 2004) favors accumulation of particles above the city. This building up of aerosol concentrations is amplified in October by the transport towards Cairo of the aerosol plume produced by the massive burning of agricultural waste in the Nile delta. This is the period when a thick, dark pollution cloud nicknamed "black cloud" by local population can be observed with the naked eye. Because of its potential health effects, the persistence of high levels of particulate concentration over Greater Cairo is a matter of great concern for its inhabitants and decision makers.

2.2. Measurements and products

2.2.1. The Sun/Sky radiometer and its direct measurements

The effect of aerosols on radiative transfer is proportional to the amount of particles present in the column but it also depends on their intrinsic optical properties (extinction efficiencies, single scattering albedo, and asymmetry parameter). The electromagnetic theory shows that these properties depend on wavelength and on the size distribution, shape, and complex refractive index of the air-suspended particles. Documenting these properties was one of the aims of the CACHE experiment carried out in Cairo between 2004 and 2006. Among the many instruments implemented at different experimental sites, two Sun/Sky radiometers (CIMEL) were operated successively from 29 October 2004 to 31 March 2006. The first instrument was operated on the premises of Cairo University (Giza, 30.026° N, 31.207° E) until 14 April 2005 and was replaced afterward by another identical instrument operated at the headquarters of the Egyptian Meteorological Authority (EMA) located just a few kilometers away from the previous site. Both instruments were incorporated in the AERONET program and the data collected at the two sites (Cairo_University and Cairo_EMA) are available online at http://aeronet.gsfc.nasa.gov/. AERONET is an extensive ground-based remote sensing aerosol network whose purpose is to measure aerosol optical properties directly and validate satellite retrievals of these properties (Holben et al., 1998). In this study we use the version 2/level 2 of the quality assured AERONET data and the corresponding inversion products. Basically, the CIMEL Sun/Sky radiometers used during CACHE measured 1) the direct Sun radiance in five spectral channels (440, 670, 870, 940 and 1020 nm) and 2) the diffuse sky radiance in the solar almucantar at four wavelengths (441, 677, 869 and 1018 nm). After pre- and post-deployment calibrations of the instruments, these solar extinction measurements are used to derive directly the AOD at all wavelengths except the 940-nm channel dedicated to the retrieval of the amount of precipitable water (PW, in cm^3/cm^2). The spectral dependence of the measured AOD contains some information on the size of particles (Junge, 1955; Pandithurai et al., 1997; Remer et al., 1999). Indeed, the measured AOD values can be fitted by Ångström's power law (Ångström, 1964) to determine the value of Ångström's exponent (α), which quantifies the spectral dependence of the AOD. Practically, α decreases when particle size increases. If a theoretical maximal value of 4 is obtained in the visible spectrum for scattering by molecules (Rayleigh scattering) values smaller than 2.0 are usually obtained for atmospheric aerosols. The value of Ångström exponent's can even become negative in the case of desert dust particles that are particularly coarse (Cerf, 1986). In combination with the AOD, the sensitivity of α to the size of particles has been used to discriminate aerosol types at several particular locations (Kaskaoutis et al., 2007 at Alta Floresta (Brazil), Ispra (Italy) and Solar Village (Saudi Arabia); El-Metwally, 2008 in Cairo). In the last case, the authors have been able to sort observations in 4 categories: 3 situations dominated by one among three different types of aerosols (desert dust or DD, biomass burning or 'pollution', and 'background'), and mixed cases in which none of the 3 previous aerosol types is clearly dominant. DD is considered to dominate when the AOD is larger than 0.7 and α less than 0.5. Biomass burning episodes correspond to AOD also >0.7 but $1.0<\alpha<1.5$, and finally background cases are defined by an AOD <0.7 and $\alpha>1.5$.

2.2.2. Products obtained by data inversion

Besides the information contained directly in the AOD and its spectral dependence, an inversion algorithm developed by Dubovik and King (2000) and subsequently modified by Dubovik et al. (2002b) can be used to retrieve the columnar aerosol's characteristics from the direct Sun and diffuse sky radiance measurements. In the most recent version (Version 2.0) of the inversion algorithm (Dubovik et al., 2006) a spheroid mixture is used as a generalized aerosol model (representing spherical, non-spherical, and mixed aerosols) in replacement of the spherical and spheroid models used separately in previous versions. Among the retrieved characteristics there is the vertically averaged aerosol volume size distribution ($dV/d\ln r$) in a range of radii between 0.05 and 15 μm. This distribution $v(r)$ can be represented by a sum of n lognormally distributed populations:

$$v(r) = \frac{dV(r)}{d(\ln r)} = \sum_{i=1}^{n} \frac{C_{v,i}}{\sigma_i (2\pi)^{1/2}} exp\left(-\frac{[\ln(r/r_{m,i})]^2}{2\sigma_i^2}\right). \quad (1)$$

In this expression, $v(r)$ and the amplitude of each population ($C_{v,i}$) are volume concentrations per cross section for an atmospheric column, r is the aerosol radius, $r_{m,i}$ is the volume geometric mean radius (gmr) and σ_i is the geometric standard deviation (gsd) for each mode. These parameters of the lognormal particle populations can be obtained by using a least square routine minimizing the difference between the volume of particles retrieved in each size class using the direct sun radiances and diffuse sky radiances measured by the CIMEL sunphotometer and the

volumes calculated using the theoretical expression represented by Eq. (1). At each of the four wavelengths, the inversion procedure also provides 1) the real and imaginary parts of the aerosol complex refractive index, 2) the scattering phase function, which in turn allows computation of the asymmetry parameter (g), and 3) the single scattering albedo (SSA). These last two quantities are crucial inputs for the radiative transfer codes used for the quantification of the aerosol's impact on radiative transfer.

Another important addition in the Version 2.0 inversion products is that a new set of radiative properties are given at any AERONET station. In particular, the solar downward ($F\downarrow(\lambda)$), and upward ($F\uparrow(\lambda)$) spectral fluxes calculated for the times of the sunphotometer measurements are provided for both the bottom and the top of the atmosphere (BOA and TOA, respectively). The instantaneous broadband downwelling ($F\downarrow$) and upwelling ($F\uparrow$) fluxes integrated over the 0.2–4.0 μm range are also available along with their values in the absence of aerosols ($F^0\downarrow$ and $F^0\uparrow$, respectively). All the broadband fluxes are simulated using an interpolation/extrapolation of the real and imaginary parts of the complex refractive index retrieved at the AERONET wavelengths. Similarly, spectral dependence of surface reflectance is interpolated/extrapolated from surface albedo values assumed in the retrieval on the wavelengths of Sun/Sky radiometer. The gaseous absorption is accounted for using the radiative transfer model GAME (Global Atmospheric ModEl) (Dubuisson et al., 1996). This model performs spectral integration using correlated-k distribution based on line by line simulations (Scott, 1974). Note that the retrieval of the broadband fluxes has been validated by comparing the calculated fluxes with results of direct ground level measurements (García et al. 2008).

The instantaneous aerosol radiative forcing (RF) and aerosol radiative forcing efficiency (FE), which allow the study of the radiative effects for the global aerosol or for more specific aerosol cases, are also available on the AERONET website.

The aerosol radiative forcing is defined as the difference between the net (downward–upward) broadband solar irradiances with (F_N) and without (F^0_N) aerosols. For instance, but this definition also applies to other atmospheric levels, the radiative forcing at BOA is given by:

$$RF_{BOA} = F_{N,BOA} - F^0_{N,BOA}. \quad (2)$$

The radiative forcing for the atmosphere (RF_{ATM}) can be derived from the radiative forcings at TOA and BOA:

$$RF_{ATM} = RF_{TOA} - RF_{BOA}. \quad (3)$$

Basically, RF_{BOA} represents the combined effects of scattering and absorption of solar radiation by air-suspended particles on the net flux at the surface, RF_{TOA} accounts for the reflection of solar radiation to space by aerosols, and RF_{ATM} for the absorption of solar radiation within the atmosphere due to absorbing particles (e.g., Mallet et al., 2006). With the sign criteria adopted here, negative values of RF correspond to an aerosol cooling effect and positive values to warming.

The aerosol radiative forcing efficiency, defined as the rate at which the atmosphere is forced per unit of aerosol optical depth taken at a reference wavelength (550 nm, in this work) can be calculated at both BOA (and TOA) with:

$$FE_{BOA} = RF_{BOA} / AOD_{550}. \quad (4)$$

Because the influence of aerosol load has been normalized in the definition of FE, its magnitude allows relatively easy comparison of the direct radiative effects of different types of aerosols, each of which is generally characterized by a specific size distribution and chemical composition. However, it must be kept in mind that the values of the instantaneous radiative forcings, and therefore the forcing efficiency defined by Eq. (4), also depend on the solar zenith angle (SZA). As a result, comparison of the FE values for different aerosol types must be made for similar ranges of SZA values.

The net atmospheric forcing given by Eq. (3) represents the amount of radiative flux absorbed by the atmosphere due to the presence of aerosols. This energy is converted into heat inside the layers containing the absorbing particles, which results in an increase of their temperature and alters regional climate (e.g., Ramanathan et al., 2007; Pilewskie, 2007). Using the basic laws of thermodynamics, the derivation of the temporal rate of this increase (atmospheric heating rate, or AHR) is straightforward (Liou, 2002):

$$\frac{\partial T}{\partial t} = \frac{g}{c_p}\frac{\Delta F}{\Delta P}. \quad (5)$$

In this equation, $\frac{\partial T}{\partial t}$ is the heating rate (in K/s, or more conveniently in K/d), g is the acceleration caused by gravity (9.8 m/s^2), c_p is the specific heat capacity of air at constant pressure (1006 Jkg^{-1} K^{-1}), and ΔP is the height of the column containing the aerosol particles expressed as the difference of atmospheric pressure between its bottom and its top. Since the distribution of the aerosol along the vertical has not been measured in the experiments, we will make the simple and classical assumption that aerosol particles are confined inside the atmospheric boundary layer. The height of this assumedly homogeneous layer can be approximated using the measurements of 1) AOD performed with the sunphotometer and 2) optical properties (scattering coefficient and single scattering albedo) performed at the surface during CACHE. The details of this derivation are not in the scope of this work but the 'scale height' obtained by this method is 2.1 ± 1.3 km (for 37 cases). This height corresponds to a pressure difference ΔP of approximately 200 hPa, the value that will be retained for the computations of the present work. Note that this scale height is similar to the one used by McFarlane et al. (2009) for Niamey (Niger) and within the range of values (1–3 km) used by Mallet et al. (2005), Moorthy et al. (2005), Roger et al. (2006), and Saha et al. (2008) in their respective studies.

3. Results and discussion

3.1. General overview of the measurement period

Among the measurements performed by the Sun/Sky photometers in the period extending from the end of October

2005 to the end of March 2006, 771 meet the AERONET level 2 quality criteria and were submitted to the data inversion treatment. Note that, because the accuracy of the AERONET inversions is optimal at solar zenith angles (SZA) larger than 45°, the available instantaneous data correspond to a rather limited range of SZA (between 50 and 76°). Among them, 23 situations neatly dominated by desert dust, 34 by pollution, and 68 by background aerosols can be identified using the discrimination procedure of El-Metwally et al. (2008). The majority of the cases, which is to say the 646 remaining ones, correspond to mixed situations in which none of the previous aerosol type is clearly dominant. The distribution of the DD, pollution, and background situations within the 12 months of the year is uneven (Table 1). The probability of observing DD situations is higher in spring since 17 of the 23 DD cases occur either in March or April but dust events can also happen in other months (1 case in Jan., 2 in Feb., and 3 in June). Biomass burning also can be observed in almost any month, but the sharp peak of October demonstrates that this activity is mostly seasonal.

These observations are consistent with previous analyses of the aerosol variability in Cairo (Alfaro and Abdel Wahab, 2006; Favez et al., 2008; Mahmoud et al., 2008; El-Metwally et al., 2008). Traffic and industrial activities inside the city itself or in its vicinity constitute a major source of particles active all year round. They contribute to the maintenance of a dense particle cloud above the city. Meteorological factors, such as rain events more frequent in the winter months can improve the situation by removing particles from the atmosphere (wash-out process) but they can also worsen it in summer when the absence of rain and high atmospheric stability favor the accumulation of particles produced locally in the lower atmosphere. In addition to the effect of these local sources, the frequent chained depressions (Khamsin depressions) occurring in spring (El-Fandy, 1940) can raise mineral dust in the desert and transport it towards the city. In October, this is the turn of carbonaceous particles produced by the outdoor burning of agricultural residues in the Nile delta to be transported towards the city by the prevailing north winds, and to be added to the local pollution cloud (El-Metwally et al., 2008; El-Askary et al., 2009).

The purpose of the two following sub-sections is to assess the impact of these seasonal changes of aerosol quantities, composition, and other intrinsic properties on the transfer of solar radiation. First, we will analyze precisely the variability of the monthly-averaged size distributions in order to explain the variability of the measured AOD and apportion it between the various aerosol components. In a second step, we will study quantitatively the variability of the instantaneous aerosol radiative forcing at BOA and TOA and of the atmospheric radiative forcing. In particular, we will try to correlate this variability with the one of the aerosol's characteristics.

3.2. The AOD and its apportionment between the aerosol components

3.2.1. Variability of the measured AOD and its spectral dependence

The results presented in Table 1 showed that 646 of the 771 observations correspond to mixed cases and that situations clearly dominated by any which one of the 3 individual aerosol types is more the exception than the rule. However, though limited the number of 1) desert dust events in spring and 2) biomass burning events in autumn is enough to increase significantly the monthly-averaged AOD (Fig. 1). Indeed, the AOD reaches a relative maximum ($AOD_{440} = 0.47 \pm 0.24$) in April at the exact time when its spectral dependence quantified by the means of the Ångström exponent is the lowest ($\alpha_{440-870} = 0.6 \pm 0.31$). This denotes an increase in the importance of the coarse mode in the aerosol size distribution, which is consistent with the introduction into Cairo's atmosphere of desert particles known to be located mostly in the supermicron range. This point will be developed further in the section dedicated to the study of the aerosol size distribution (see later discussion). A second AOD maximum ($AOD_{440} = 0.602 \pm 0.23$) is obtained at the October peak of the biomass burning season. Contrary to desert dust, the addition of this 'pollution' component does not alter significantly the spectral dependence of the AOD. This suggests that the size distribution of the new component is probably similar to the one of the pre-existing aerosol. Regarding the aerosol's size distribution, the fact that the maximal value of the Ångström exponent is achieved in July ($\alpha_{440-870} = 1.30 \pm 0.23$) indicates that this is also the month when the relative importance of the very fine particles in the particles' size distribution is largest. More generally, the summer period is characterized by high AOD values that can be explained in part by particularly stable atmospheric conditions. Though this cannot be ascertained by our measurements, the formation of photochemical smog (Tafuro et al., 2007) also probably contributes to the enhancement of the AOD. Conversely, a marked AOD minimum is observed in the winter months due to the cleaning of the atmosphere by rain wash-out (El-Wakil et al., 2001; Tadros et al., 2002; Zakey et al., 2004).

3.2.2. Aerosol size distribution

As a result of the variety of sources contributing to the atmospheric particle load in Cairo and as already suggested

Table 1
Numbers of cases when desert dust (DD), biomass burning (Poll.), or background (Back.) aerosols are dominating. Note that months from November to March appear twice in the measurement period running from the end of October 2004 to the end of March 2005. For allowing easy comparison with other months, the corresponding figures have been divided by 2 and are reported in italics.

	Jan.	Feb.	Mar.	Apr.	May	Jun.	Jul.	Aug.	Sep.	Oct.	Nov.	Dec.	Total
DD	*0.5*	*1*	*5*	7	0	3	0	0	0	0	*0*	*0*	23
Poll.	*0.5*	*0*	*0*	0	1	1	0	2	0	15	*3.5*	*3.5*	34
Back.	*11*	*0*	*10*	0	0	0	3	0	1	2	*2.5*	*7.5*	68
Mixed	*35*	*28.5*	*48*	82	56	37	15	31	32	17	*41*	*35.5*	646
All	94	59	126	89	57	41	18	33	33	34	94	93	771

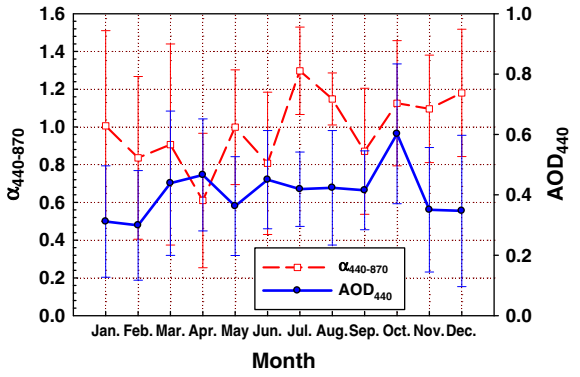

Fig. 1. Monthly means of the aerosol optical depth (at 440 nm) and of the Ångström exponent ($\alpha_{440-870}$) derived from the sunphotometer measurements performed in Cairo between Oct: 2004 and Mar. 2006.

earlier by the study of the spectral dependence of the AOD, the size distribution of the aerosol is found to be highly variable from one month to the other (Fig. 2). Because the electromagnetic theory shows that the result of particle/radiation interactions depends strongly on the size factor, i.e. on the ratio of the aerosol size to the incident wavelength, it is important to assess accurately the temporal variability of the characteristics of the aerosol size distribution. In first approximation, it seems that the month averages of the volume size distributions are bimodal and that the amplitude of the two modes increases with the AOD. However, a closer examination of the size distributions of some particular months (e.g., June and September) suggests that 3 particles populations, and not just 2, might be necessary to account for the complexity of the measured size distributions. More precisely, if one very fine mode (VFM) of particles is observed in all seasons and does not seem to change much in position, the size distribution of the particles located in the super-micron range is more variable. Indeed, the maximum of the coarse peak is located around 2 μm in March, April, and June but between 4 and 5 μm in May, August, July or October, for instance. In addition, the shape of the size distribution above 1 μm for the months of June and May clearly reveals that 2 populations of particles coexist in the coarse range of sizes. All these semi-quantitative observations are confirmed by the results of the iterative procedure used to fit lognormal populations to the month-averaged sized distributions (Fig. 3 illustrates the quality of this fit for 2 months). Indeed, 3 populations are required to account for the size distributions of all months but March and April. The finest population corresponds to the VFM already defined earlier and has a gmr of 0.15(±0.01)μm and a gsd of 1.54(±0.11). This low gmr value is typical of the accumulation mode. In the coarse range, 2 populations with gmrs of 2.60(±0.17) and 4.72(±0.50)μm, and respective gsds of 2.03(±0.16) and 1.41(±0.12), are obtained. The finer of these 2 coarse modes will be hereinafter referred to as the desert dust mode (DDM) because its importance is particularly marked in March and April (Table 2). Note that the desert dust origin of the DDM is further supported by the strong correlation linking its

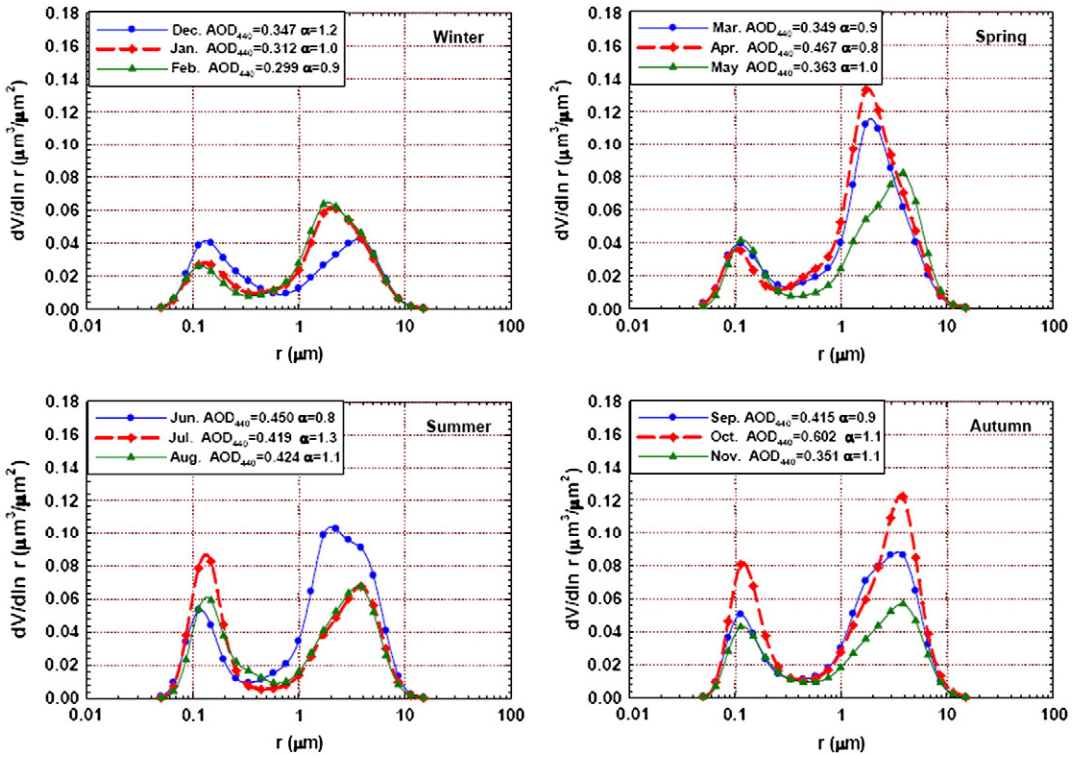

Fig. 2. Monthly-averaged size distributions obtained by inversion of the sunphotometer data collected in the winter, spring, summer and autumn seasons.

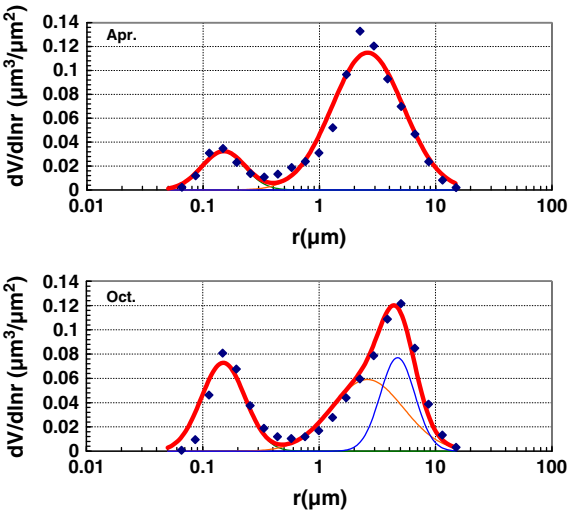

Fig. 3. The blue points represent the monthly-averaged aerosol size distributions obtained by inversion of the sunphotometer measurements performed in 2 months representative of desert dust conditions (April) and of biomass burning aerosols (October). The best fit to these measurements (red line) yielded by an iterative adjustment routine involving 3 lognormally distributed particle populations (VFM, DDM, and BBM) is also represented (see text for details).

amplitude (C_{DDM}) with the number (N_{DD}) of DD cases observed in each month.

$$C_{DDM} = 0.019N_{DD} + 0.08 \quad \left(R^2 = 0.80; n = 12\right) \tag{6}$$

This linear equation with a vertical intercept ($C_{DDM} = 0.08$ for $N_{DD} = 0$) suggests that a significant amount of DDM particles is present above Cairo even in the months when no typical desert dust event is observed. This is consistent with the results of the chemical analyses performed by Favez et al. (2008) who had found that mineral particles were in all seasons an important component of the background aerosol in Cairo. The presence of this dust component in the atmosphere outside the dust storm periods can be explained by the remobilization by various human activities (traffic, construction sites…) of material deposited previously.

Table 2
Amplitudes (in $\mu m^3/\mu m^2$) of the 3 populations of lognormally distributed particles (VFM, DDM, and BBM) that best fit the month-averaged volume size distributions derived from the sunphotometer measurements.

Month	VFM	DDM	BBM
Jan.	3.12E−02	1.01E−01	1.84E−03
Feb.	2.81E−02	1.10E−01	1.51E−04
Mar.	4.19E−02	1.75E−01	0.00E+00
Apr.	3.49E−02	2.04E−01	0.00E+00
May	4.12E−02	9.10E−02	4.00E−02
Jun.	5.26E−02	1.61E−01	2.57E−02
Jul.	8.26E−02	6.20E−02	4.04E−02
Aug.	6.05E−02	7.08E−02	3.52E−02
Sept.	5.04E−02	1.22E−01	3.22E−02
Oct.	7.86E−02	1.05E−01	6.62E−02
Nov.	4.54E−02	6.34E−02	2.91E−02
Dec.	4.55E−02	4.73E−02	2.10E−02

The second coarse mode achieves its maximal amplitude in October at the peak of the biomass burning period. Because of this correlation it will be referred to as the biomass burning mode (BBM). Note that a coarse mode associated with biomass burning had already been reported in the literature, for instance by Remer et al. (1998) who measured the size distribution of such aerosols in the Amazon basin. In Cairo, BBM is almost completely absent from the atmosphere from January to April showing that, unlike desert dust, it is not a permanent component of the city's atmosphere. Finally, the importance of the accumulation mode is found to be more or less constant from November to May ($3.83 \pm 0.69E{-}02\ \mu m^3/\mu m^2$) but it increases in the summer months to reach a peak in July. This could be due to photochemical processes particularly active at this time of year and constituting a new source of very fine particles adding its effects to those of more regular activities (traffic, industry…). Biomass burning is also responsible for a dramatic increase of the amplitude of the VFM in October. In summary, this agricultural activity seems to produce at the same time very fine and very coarse particles (BBM). The fact that the Ångström exponent is not significantly altered in October could be the result of a compensation effect between the simultaneous emissions of these very fine and very coarse particles.

In summary, the accumulation mode (VFM) is produced in part by the 'background' activities such as industry and traffic, in part by the biomass burning, and possibly by photochemistry in the summer months. The intermediate coarse mode (DDM) is associated with desert dust. Its amplitude is enhanced in the months when dust storms are more likely to occur, but due to the remobilization of deposited dust by urban activities this mineral component always constitutes a significant share of the global aerosol. Finally, the very coarse mode (BBM) seems to be associated with the biomass burning activities, which enhance at the same time its amplitude and the one of VFM.

3.2.3. Variability of intrinsic optical properties (SSA and g)

The variation with time of the size distribution and composition of the aerosol is reflected by changes in its optical properties. In order to illustrate this point we can compare the month-averages of the spectral single scattering albedo and asymmetry parameter yielded by the inversion algorithm for several contrasted months. Fig. 4 displays the cases of April, July, October, and December, which have been selected for being representative of the influence of desert dust, photochemical smog, biomass burning, and background aerosols, respectively. At 441 nm, the SSA values are in the same order of magnitude (0.89 ± 0.07) for the 4 months but the spectral pattern is different. In April, SSA increases with λ – a behavior typical of mineral dust (e.g., Kaufman et al., 2001; Tanré et al., 2001; Dubovik et al., 2002a; Derimian et al., 2006)– to reach values slightly larger than 0.90. These relatively high values show that, except at 441 nm where iron-oxide minerals contained in the dust particles enhance their absorbing power (e.g., Sokolik and Toon, 1999; Alfaro et al., 2004), desert dust is a poor absorber of solar radiation. However, it must be noted that the SSA values obtained by Derimian et al. (2006) for desert dust cases over Sede Boker (Israel) were even larger (0.96–0.98) at comparable wavelengths. The lower SSA of DD in Cairo could be due to their mixing with strongly absorbing (carbonaceous) species always present in the area.

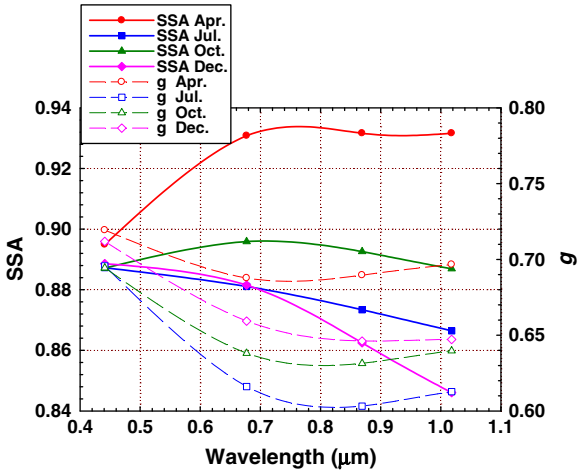

Fig. 4. Spectral dependence of the single scattering albedo (SSA) and asymmetry parameter (g) obtained by inversion of the sunphotometer data collected during 4 months representative of: 1) desert dust (April), 2) aerosols produced by photochemical processes (July), 3) biomass burning (October), and 4) background activities (December).

Conversely, the decrease of SSA with λ observed in the other 3 months is characteristic of aerosols rich in this carbonaceous component. The decrease steeper in July and December than in October, when SSA is practically independent of λ, is also consistent with the fact that the origin of the carbonaceous particles is not the same in this month than during the rest of the year. Indeed, biomass burning particles do not only have a size distribution richer in coarse particles (see earlier discussion), but they are also known to be less absorbing on the large wavelength-side of the solar spectrum than the ones produced by car engines or by industrial processes (e.g., Andreae and Gelencser, 2006).

The difference in aerosol size for the 4 months used in the comparison is also visible on the values of the asymmetry parameter. The smallest g values are obtained in July because in this month the photochemical production of particles in the accumulation mode increases the amplitude of the VFM population. Conversely, the largest values of g are observed in April, which is to say when the proportion of coarse particles in the aerosol is maximal. Note that October is an intermediate case, in the sense that biomass burning enhances at the same time the amplitudes of the coarsest (BBM) and finest (VFM) particle populations.

3.2.4. Apportioning the AOD between the 3 particle modes

Because the three populations of particles identified in the size distribution analysis are linked to different generation processes and aerosol types, it is interesting to assess their individual contribution to the overall AOD measured by the sunphotometer. This AOD can be considered as the sum of the 3 contributions and expressed as follows:

$$\mathrm{AOD} = \sum_{1}^{3} C_i E_i. \qquad (7)$$

In this expression, C_i is the amplitude (in $\mu m^3/\mu m^2$) of mode i (VFM, DDM, or BBM) in the volume size distribution and E_i is its volume extinction efficiency (in $\mu m^2/\mu m^3$), so that the products C_iE_i are the dimensionless fractions of AOD corresponding to each particle mode.

Assuming that the E_i values remain constant along the year for each mode, the 12 values of the month-averaged AODs and the corresponding C_is (see Table 2) provide 12 sets of data that must satisfy simultaneously Eq. (7) in which the E_is are the unknown. An iterative minimizing routine can be used to determine the values of the 3 extinction efficiencies that provide the best agreement between the 12 measured AODs and those derived from Eq. (7). At the wavelength of 440 nm, the values of E_i yielded by this method are 3.84, 1.59, and 1.61 $\mu m^2/\mu m^3$ for VFM, DDM, and BBM, respectively. The quality of the AOD retrieval is attested by the good correlation between the calculated and measured AODs ($AOD_{cal} = 1.08 AOD_{mes} - 0.04$; $R^2 = 0.87$, $n = 12$).

With the E_i values, it is now possible to compute the individual contributions (C_iE_i) of the 3 modes of particles to the total AOD_{440}. The results (Table 3) show that the contribution of BBM to AOD_{440} is always less than 0.06 except in October when it reaches 0.11, which is to say approximately 20% of the total. On a yearly basis, BBM accounts for 9% of the AOD. Conversely, the VFM and DDM modes represent 47 and 43% of the AOD, respectively. In April, AOD_{DDM} reaches its maximal value (0.33) and explains 71% of the total AOD for this month. Similarly large values (0.32 and 0.30) of individual contributions to the AOD are obtained for VFM in July and October, respectively. As already mentioned, photochemistry most probably contributes to the July peak, whereas the advection of biomass burning particles to Cairo is responsible for the October one. If one considers that the enhancement of AOD_{BBM} and AOD_{VFM} in October relative to the surrounding, 'business as usual' months (September and November) is due to biomass burning particles, it can be estimated that the total increase of AOD due to this process is 0.18, 0.12 of which are due to VFM and 0.06 to the coarse mode (BBM). This enhancement is in the same order of magnitude as the one due to the dust events of April and estimated by comparing the AOD_{DDM} for this month (0.33) with the one (0.15) of the following month (May) during which no dust event was observed (see Table 1).

Table 3
Monthly means of the AOD measured at 440 nm by the sunphotometer and its apportionment between the 3 particle modes (VFM, DDM, and BBM) identified in the size distribution analysis. The year averages of these contributions and the corresponding standard deviations (SD) are also reported.

	AOD_{mes}	AOD_{VFM}	AOD_{DDM}	AOD_{BBM}	AOD_{cal}
Jan.	0.31	0.12	0.16	0.00	0.28
Feb.	0.30	0.11	0.17	0.00	0.28
Mar.	0.44	0.16	0.28	0.00	0.44
Apr.	0.47	0.13	0.33	0.00	0.46
May	0.36	0.16	0.15	0.06	0.37
June	0.45	0.20	0.26	0.04	0.50
Jul.	0.42	0.32	0.10	0.06	0.48
Aug.	0.42	0.23	0.11	0.06	0.40
Sept.	0.42	0.19	0.19	0.05	0.44
Oct.	0.60	0.30	0.17	0.11	0.58
Nov.	0.35	0.17	0.10	0.05	0.32
Dec.	0.35	0.17	0.08	0.03	0.28
Year av. (SD)	0.41(0.08)	0.19(0.06)	0.17(0.08)	0.09(0.04)	0.40(0.10)

3.3. Instantaneous radiative forcing and heating rate

3.3.1. Statistical distribution of the radiative forcing for the whole period

The inversion of the 771 measurements provides an equal number of instantaneous radiative forcing values at both BOA and TOA. The frequency distributions of RF_{BOA} and RF_{TOA} both follow (Fig. 5) the classical Gaussian law. At BOA and TOA, the mean radiative forcing (RF_m) and associated standard deviation (SD) are $-58(\pm 27)$ and $-19(\pm 11)W/m^2$, respectively. The scatter of the values around the mean values can be attributed in part to the variability of the aerosol integrated content (AOD) and in part to the variability of the aerosol characteristics (see later discussion). Note that, even though the range of solar zenith angles is rather limited (50–76°), differences in SZA between the individual cases must also contribute to this scatter. In any case, the negative values of the radiative forcings correspond to a cooling effect at both the BOA and TOA. More precisely, the negative RF_{BOA} means that less energy is able to reach the surface due to the scattering and absorbing effects of the aerosol (this situation corresponds to a 'dimming' at ground level), and the negative RF_{TOA} means that more solar light is backscattered to space because of the aerosol. In general, RF values at TOA over Cairo are relatively high if compared for example to the values measured in the polluted and dusty environment of Yulin (China) by Che et al. (2009) and at La Valette (France) by Saha et al. (2008). This means that the aerosol in Cairo reflects more solar radiation to space, which is probably due to the fact that the proportion of desert dust in the aerosol is always large (see earlier discussion).

On average, RF_{BOA} in Cairo is 3 times larger than RF_{TOA}. The difference between the RF values at TOA and BOA (RF_{ATM}) represents the amount of solar energy converted into heat inside the atmosphere and is a good indicator of the aerosol's effects on the atmospheric dynamics (Miller et al., 2004; Tafuro et al., 2007). The value of 39 W/m^2 for RF_{ATM} corresponds to an estimated instantaneous heating rate of 1.6 K/d. By evaporating low-level clouds this heating of the lower part of the atmosphere could result in a decrease of both cloud cover and planetary albedo (Hansen et al. 1997; Ackerman et al. 2000) and hence have a considerable effect on the regional climate.

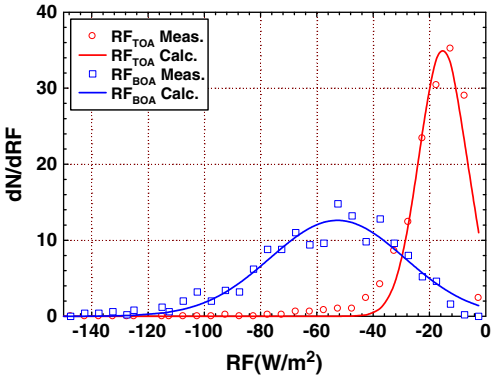

Fig. 5. Frequency distribution of the radiative forcing at TOA and BOA using the entire set of sunphotometer data collected during the CACHE experiment. The Gaussian best fits to the measurements are also represented.

The comparison of the standard deviations of the RF distributions shows that the effect of the aerosol is more variable at the surface than at TOA. Naturally, the largest values of the aerosol radiative forcing are due to the more severe cases of atmospheric particle loadings. For instance, during the dust event of April 8, 2005 ($AOD_{440}=1.09$ at 6:30 AM, GMT; SZA = 52.9°), the values of RF_{BOA} and RF_{TOA} were -161.7 and -65.9 W/m^2, respectively. At almost exactly the same SZA (51.8°), the somewhat less intense biomass burning case of October 25, 2005 ($AOD_{440}=0.72$ at 11:41 GMT) led to RF values of -113.0 and -29.7 W/m^2 at BOA and TOA, respectively. On these extreme occasions, the instantaneous atmospheric forcing was maximal (95.9 and 83.8 W/m^2 for the dust and biomass burning cases, respectively) and so were the corresponding heating rates (4 and 3.5 K/d). These heating rates are slightly lower than the one (5 K/d) estimated for an extremely intense desert dust event observed in Niamey (Niger) by Mc Farlane et al. (2009) but larger than the 2.5 K/d value of a dust-dominated case in New Delhi (India) (Pandithurai et al., 2008) or than the 2.8 K/d of an intense pollution episode monitored over Marseilles (France) by Roger et al. (2006). More generally, the largest values of the RF_{BOA}, RF_{TOA}, and heating rates are observed in Cairo during the dust and pollution cases. This is primarily due to the fact that these events are associated with the largest AODs (Table 4).

3.3.2. Forcing efficiencies

By definition, the radiative forcing at any atmospheric level (in particular BOA and TOA) increases directly with the AOD. The value of the proportionality constant (FE) involved in this relationship depends on the SZA but also on the scattering and absorbing properties of the aerosol, which are themselves linked to its intrinsic characteristics (size distribution, more or less complex composition etc.). Due to the variability of these characteristics and of the SZA, the distributions of the FE_{BOA} and FE_{TOA} values obtained by dividing the whole set of 771 individual radiative forcings by the coinciding AOD_{550} are characterized by a certain width. It can be seen on Fig. 6 that the FE values are distributed according to the normal (Gaussian) law. For FE_{BOA} and FE_{TOA}, the means ($\pm$SD) of the Gaussian distributions are -195 ± 42 and -62 ± 17 W/m^2, respectively (Table 4). As already discussed earlier, the majority (646/771) of the observations correspond to mixed aerosol cases in which neither the desert

Table 4
Aerosol optical depth at 440 nm (AOD_{440}), radiative forcings at BOA and TOA (in W/m^2), and associated forcing efficiencies (relative to AOD_{550}) for situations dominated by individual aerosol types (desert dust, biomass burning, and background aerosols) or averaged over the whole period of study (All data). Note that the measurements correspond to solar zenith angle values varying between 50 and 76°. The atmospheric heating rate (AHR, in K/d) is also indicated.

Parameters	Dust	Pollution	Background	All data
AOD_{440}	0.96 ± 0.19	0.85 ± 0.15	0.32 ± 0.15	0.39 ± 0.21
RF_{BOA}	-121 ± 34	-99 ± 24	-45 ± 21	-58 ± 27
RF_{TOA}	-57 ± 13	-32 ± 7	-13 ± 6	-19 ± 11
AHR	2.7 ± 1.1	2.8 ± 0.9	1.3 ± 0.8	1.6 ± 0.8
FE_{BOA}	-129 ± 23	-155 ± 29	-204 ± 43	-195 ± 42
FE_{TOA}	-61 ± 7	-50 ± 8	-64 ± 18	-62 ± 17
FE_{ATM}	69 ± 22	104 ± 28	140 ± 54	134 ± 50

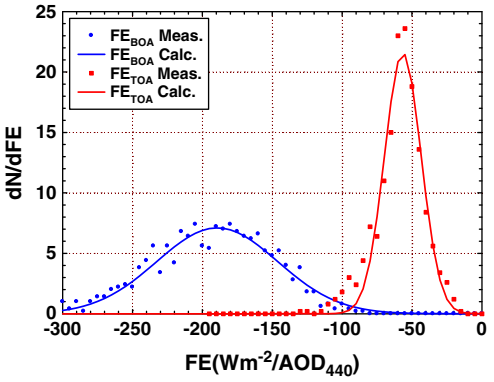

Fig. 6. Frequency distributions of the forcing efficiencies retrieved at TOA and BOA using the entire set of sunphotometer data.

dust nor the biomass burning component is really dominant. It is possible to study the effect of these two components, and also of the background aerosol, on the transfer of solar radiation by isolating the corresponding occurrences in the complete set of available data. Though the number of typical DD, pollution, and background situations is rather limited (23 for DD, 34 for pollution, and 68 for background), the distributions of their forcing efficiencies are also found to be Gaussian. Table 4 displays the average values of these forcing efficiencies at BOA and TOA along with those already calculated previously using all data. At TOA, the FE averaged over the whole data set is not significantly different from the one found for the background aerosol alone (-62 ± 17 vs -64 ± 18 W/m^2.AOD$_{550}$). This shows that on average the normalized effect of the aerosol on solar radiation is the same as the one of the background aerosol produced by routine activities inside the city. In good agreement with the compositional analysis performed at ground level (Favez et al., 2008; Mahmoud et al., 2008), the low SSA values and the spectral dependence of the month most representative of the background aerosol (December, on Fig. 4) suggest that this aerosol is relatively rich in absorbing carbonaceous species. However, comparison with results obtained in Yulin (China) by Che et al. (2009) shows that the forcing efficiency at TOA is larger in Cairo (-62 as compared to -29.9 W/m^2. AOD$_{440}$). This relatively large FE$_{TOA}$ in the Egyptian capital indicates that there the aerosol backscatters more solar radiation to space than in Yulin. This is probably due to the desert dust component of the aerosol, whose importance in Cairo's atmosphere has been attested for all seasons by the chemical analyses of Favez et al. (2008) and by our previous apportionment of the AOD showing that mineral dust alone accounts for at least 21% of AOD$_{440}$ (in July), and up to 71% (in April).

At BOA also, the values of FE for the whole period are similar to those of the background aerosol (Table 4). The generally marked absorbing character of the aerosol is denoted by the importance of the difference between the FE at BOA and TOA (FE$_{ATM}$) in usual (all cases) conditions. However, departures from this rule are observed during both the biomass burning and the desert dust events. Indeed, the relatively small values of FE$_{BOA}$ during the intense 'pollution' episodes mean that for the same AOD the biomass burning aerosol induces a radiative forcing at the surface lower than the one due to the aerosol produced by regular traffic and industrial activities. This could be explained by a lower absorbing potential of the biomass burning aerosol vis a vis solar light, as demonstrated by the values (Fig. 4) of the SSA which are larger in the month dominated by biomass burning (October) than in those dominated by background aerosols (e.g., December). The forcing efficiency at BOA is also smaller in situations dominated by desert dust than during the background, or the average, conditions. This lower value was expected for mineral dust that is known to be less absorbing than urban aerosols (Kim et al., 2005; Saha et al., 2008). Note that though in the same order of magnitude the average value of FE$_{BOA}$ for desert dust is slightly lower than for biomass burning (Table 4). This is confirmed by the examination of the variations of FE$_{BOA}$ and FE$_{TOA}$ with SZA (Fig. 7) showing that for SZA between 50 and 76° FE$_{BOA}$ is approximately 20% smaller than for the biomass burning aerosol. The fact that two completely different aerosols cause relatively comparable solar light reduction at ground level could be the result of a compensation effect between the large absorption and low scattering of the biomass burning aerosols on the one side, and of the large scattering and low absorption of desert dust on the other side. The forcing of desert dust at BOA can also be compared with the ones reported by Kim et al. (2005) for 3 East Asian sites. Though East Asian dust is often mixed with urban aerosol from China, the corresponding surface FE values (from -91 to -106 W/m^2.AOD$_{550}$) are lower than in Cairo. This suggests that the influence of the absorbing urban component is larger in Cairo than in East Asia, and this even during the events assumedly dominated by mineral dust. Finally, it must be kept in mind that, in spite of the smaller values of FE$_{BOA}$ for the desert dust and biomass burning aerosols, situations dominated by these two kinds of aerosols are the ones which lead to the largest values of the BOA and TOA forcings, simply because of the very large atmospheric loadings (AOD) that characterize them. Also note that due to their different optical properties, mineral dust particles induce a normalized atmospheric forcing (FE$_{ATM}$ = 69 W/m^2) two times smaller than the one (FE$_{ATM}$ = 140 W/m^2) of the background aerosol, which emphasizes again the largest heating potential of this carbon-rich aerosol.

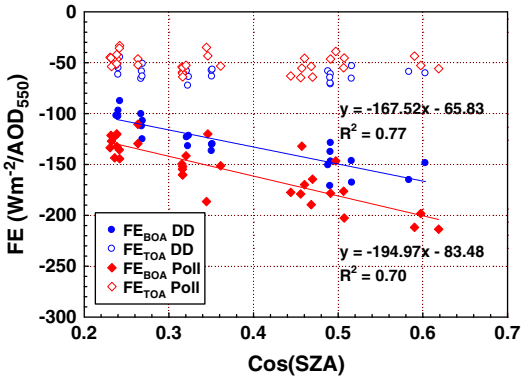

Fig. 7. Influence of the solar zenith angle (SZA) on the forcing efficiencies at TOA and BOA for the desert dust– (DD) and biomass burning– (poll) dominated cases.

3.3.3. Seasonal variability

The results detailed earlier show that in spite of their different compositions and size distributions the desert dust and 'pollution' aerosols induce comparable forcing efficiencies at BOA but that these normalized forcings are smaller than those of the more absorbing 'background' and 'mixed' aerosol types. Due to the smoothing effect of averaging over periods of one month, these differences are no longer visible on the FE_{BOA} values reported in Table 5. Indeed, the standard deviation of the month averages ($16\ W/m^2.AOD_{550}$) represents only 8% of the annual mean ($-191\ W/m^2.AOD_{550}$), which is notably less than the average in-month variability of the instantaneous measurements ($21 \pm 3\%$). Similarly, the month to month variability of the forcing efficiency is relatively small at TOA ($6.9\ W/m^2.AOD_{550}$, or 11% of the $62\ W/m^2.AOD_{550}$ average value) when compared to the 25% of the in-month variability. This suggests that the impact of the desert dust and biomass burning aerosols on the forcing efficiencies at TOA and BOA could be important at short timescales, typically of the order of a few days.

However, because it reflects also the month to month variability of the aerosol concentration (or AOD) and not only the one of the aerosol intrinsic properties, but also the radiative forcing at both BOA and TOA is more fluctuating (17 and 20%, respectively) than the forcing efficiencies. Assuming that the radiative forcing variations due to changes in aerosol content should be in great part controlled by the fluctuations of the amplitudes of the more variable components, namely DDM and BBM whose influence on the AOD has already been assessed earlier, a simple linear expression can be proposed for RF:

$$RF = RF_0 + A_{DDM}C_{DDM} + A_{BBM}C_{BBM}. \quad (8)$$

In this equation, RF_0 (in W/m^2) represents the average radiative forcing in the absence of DDM and BBM modes and for the limited range of SZA (50 to 76°) represented in our data set. A_{DDM} and A_{BBM} (in $W/m^2/\mu m$) are the sensitivities of RF to fluctuations of the amplitudes (C_{DDM} and C_{BBM}) of the dust and biomass burning modes.

Using the monthly C_{DDM} and C_{BBM} of Table 2, it is possible to determine the values of RF_0, A_{DDM}, and A_{BBM} (-30.7, -170.6, -361.5, and -8.1, -77.0, -89.7, for BOA and TOA, respectively) yielding the best agreement of the RF calculated according to Eq. (8) with the month averages of the AERONET retrievals. At BOA and TOA, this method gives the results displayed in Table 6. The quality of the retrieval is denoted by the good agreement between the recalculated RF (RF_{cal}) and the measured forcings (Table 6). This good agreement obtained using the simple linear Eq. (8) supports our initial assumption that the modulation of the month average of the radiative forcing measured in the 50–76° range of SZA is mostly due to the variability of the DD and BB components. More quantitatively, examination of the relative contributions of the desert dust and biomass burning modes to the recalculated forcings confirms the importance of DD in all months, and particularly in spring. Indeed, although the fractions of RF_{BOA} and RF_{TOA} due to the DDM are already relatively large in December (17 and 27%, respectively), they peak at values as high as 53 and 66% in April. The impact of biomass burning on radiative forcing is also quite variable during the year. The contribution of the BB mode is negligible in the winter months, probably because they are also those in which rain is more liable to occur and therefore not the most favorable for the burning of vegetal material. Conversely, this contribution reaches 33 and 27% at BOA and TOA, respectively, in October, which is to say when farmers of the Nile delta get rid of agricultural waste after harvest.

4. Summary and conclusion

More than one year of quality assured data collected in Cairo with a carefully calibrated sunphotometer and inverted with the latest version of the NASA-AERONET algorithm have been analyzed. Our results show that the aerosol's characteristics and its impacts on the transfer of solar radiation are highly variable in time. This high-frequency variability can be explained by the occasional addition of new components to a background aerosol produced by daily-basis activities inside the city itself. In good agreement with previous studies showing that traffic is a main source of pollution in Cairo, the radiative properties of the background particles are those of an aerosol particularly rich in absorbing carbonaceous component, and its size distribution involves a large

Table 5
Monthly averages of the instantaneous aerosol radiative forcing (RF, in W/m^2) and forcing efficiencies (FE, in $W/m^2.AOD_{550}$) at TOA and BOA. The forcing efficiency of the atmosphere (ATM), its radiative forcing and associated heating rate (AHR, in K/d) are reported along with the aerosol optical depth at 440 nm (AOD_{440}). Note that the means and standard deviations in the last line are calculated using the month averages.

Month	RF			AHR	FE			AOD_{440}
	TOA	BOA	ATM		TOA	BOA	ATM	
Jan.	-17.4 ± 9.6	-47.2 ± 23.8	29.8 ± 18.5	1.3 ± 0.8	-74.7 ± 20.7	-196.9 ± 41.0	122.3 ± 53.6	0.312 ± 0.18
Feb.	-16.8 ± 11.2	-46.9 ± 24.5	30.2 ± 19.3	1.3 ± 0.8	-70.8 ± 22.1	-202.1 ± 38.0	131.3 ± 54.4	0.299 ± 0.18
Mar.	-22.0 ± 15.0	-65.2 ± 34.4	43.2 ± 25.2	1.8 ± 1.1	-62.1 ± 16.4	-188.0 ± 38.6	126.0 ± 48.4	0.439 ± 0.24
Apr.	-24.3 ± 16.0	-70.2 ± 39.6	45.9 ± 28.8	1.9 ± 1.2	-58.6 ± 20.4	-180.7 ± 46.9	122.1 ± 43.3	0.467 ± 0.24
May	-15.4 ± 12.0	-53.3 ± 25.8	37.9 ± 13.6	1.6 ± 0.6	-54.3 ± 16.3	-197.6 ± 52.9	143.3 ± 40.9	0.363 ± 0.14
Jun.	-21.4 ± 8.0	-61.1 ± 17.7	39.7 ± 13.3	1.7 ± 0.6	-58.9 ± 10.6	-172.5 ± 32.2	113.7 ± 34.9	0.450 ± 0.16
Jul.	-15.4 ± 4.7	-56.2 ± 17.9	40.7 ± 17.6	1.7 ± 0.7	-51.3 ± 11.3	-185.5 ± 32.7	134.2 ± 38.8	0.419 ± 0.12
Aug.	-17.2 ± 7.1	-52.2 ± 17.5	35.0 ± 13.4	1.5 ± 0.6	-54.3 ± 9.5	-171.9 ± 33.3	117.6 ± 36.5	0.424 ± 0.19
Sep.	-19.6 ± 5.8	-56.1 ± 12.5	36.4 ± 11.8	1.5 ± 0.5	-59.5 ± 10.3	-174.0 ± 34.6	114.5 ± 37.7	0.415 ± 0.13
Oct.	-25.5 ± 10.4	-80.8 ± 24.7	55.3 ± 18.2	2.3 ± 0.8	-55.9 ± 10.6	-186.5 ± 38.7	130.5 ± 41.8	0.602 ± 0.23
Nov.	-14.5 ± 8.5	-55.8 ± 25.6	41.3 ± 20.3	1.7 ± 0.9	-56.0 ± 16.0	-220.3 ± 44.7	164.3 ± 53.9	0.351 ± 0.21
Dec.	-15.4 ± 9.8	-52.5 ± 27.3	37.1 ± 21.1	1.6 ± 0.9	-63.1 ± 16.9	-216.6 ± 43.1	153.5 ± 49.8	0.347 ± 0.25
mean	-18.7 ± 3.7	-58.1 ± 9.8	39.4 ± 6.9	1.7 ± 0.3	-60.0 ± 6.9	-191.1 ± 16.2	131.1 ± 15.7	0.407 ± 0.08

Table 6
Comparison of the monthly-averaged aerosol radiative forcings (RF_{TOA_calc} and RF_{BOA_calc} in W/m^2) calculated using Eq. (8) with the averages derived from the sunphotometer measurements. The contributions of the constant (RF_0), desert dust (RF_{DDM}), and biomass burning (RF_{BBM}) to the overall forcings are also reported.

Month	RF_{TOA}	RF_{TOA_calc}	$RF0_{,TOA}$ (%)	RF_{DDM} (%)	RF_{BBM} (%)
Jan	−17.4	−16.1	51	48	1
Feb	−16.8	−16.6	49	51	0
Mar	−22.0	−21.6	38	62	0
Apr	−24.3	−23.9	34	66	0
May	−15.4	−18.7	43	37	19
June	−21.4	−22.8	36	54	10
Jul	−15.4	−16.5	49	29	22
Aug	−17.2	−16.8	49	33	19
Sept	−19.6	−20.4	40	46	14
Oct	−25.5	−22.2	37	36	27
Nov	−14.5	−15.6	52	31	17
Dec	−15.4	−13.7	60%	27	14
	−18.7		45 ± 8	43 ± 13	12 ± 10
Month	RF_{BOA}	RF_{BOA_calc}	$RF0_{,BOA}$ (%)	RF_{DDM} (%)	RF_{BBM} (%)
Jan	−47.2	−48.6	63	35	1
Feb	−46.9	−49.5	62	38	0
Mar	−65.2	−60.5	51	49	0
Apr	−70.2	−65.5	47	53	0
May	−53.3	−60.7	51	26	24
June	−61.1	−67.4	45	41	14
Jul	−56.2	−55.9	55	19	26
Aug	−52.2	−55.5	55	22	23
Sept	−56.1	−63.1	49	33	18
Oct	−80.8	−72.5	42	25	33
Nov	−55.8	−52.0	59	21	20
Dec	−52.5	−46.3	66	17	16
	−58		54 ± 8	32 ± 12	15 ± 12

proportion of very fine particles located in the accumulation mode (VFM). The months most representative of this background conditions are the winter months and the corresponding aerosol optical depths are usually low (e.g., $AOD_{440} = 0.3$ in January) because the atmosphere is cleaned by the rain events which, though rare, occur mostly in this season. In summer, and most particularly in July, active photochemistry leading to formation of secondary aerosols located in the accumulation mode combines with atmospheric stability and the absence of rain to favor the building up of aerosol concentration, which in turn increases the AOD.

In October, the aerosol plume produced by the burning of agricultural residues in the Nile delta is advected towards Cairo and added to the locally produced aerosol. This new 'pollution' component not only enhances the concentration of the accumulation mode (VFM) but also of a very coarse mode clearly associated with the biomass burning (BBM). As a consequence, the largest value of the month-averaged AOD is observed in this month ($AOD_{440} = 0.6$).

Mineral dust raised by strong winds in the desert is another external component that can be added in large quantities to the locally produced aerosol. Though the probability of occurrence of dust events is largest in spring, a mineral component is present in the aerosol in all months due to the re-suspension of deposited material by human activities. The analysis of the monthly-averaged size distribution of the aerosol shows that desert dust is mainly associated with a particle mode (DDM) located in the supermicron size-range but somewhat smaller than BBM. Due to the importance of this desert dust component, the AOD measured in April ($AOD_{440} = 0.47$) is the second largest of the year. Our apportionment of the AOD between the 3 modes of the size distribution also shows that if in April DDM alone accounts for 71% of the total AOD, its contribution in other months is always larger than 20%. This makes of DD one of the main components of Cairo's atmosphere, even in the months when no major dust event is observed. The optical properties of DD are also significantly different from those of the other aerosol components. In particular, as demonstrated by its largest single scattering albedo, DD absorbs less (scatters more) solar light than the other aerosol species. As a result, the instantaneous forcing efficiency is larger at TOA, and smaller at BOA, during the periods dominated by DD than in other situations. Also noteworthy is that the biomass burning aerosol is not as absorbing as Cairo's background aerosol and is therefore characterized by a significantly lower instantaneous forcing efficiency at BOA.

Because the DD and BB outbursts are of relatively short duration, these differences in forcing efficiencies are smoothed out by the averaging of instantaneous values over periods of one month. For these longer periods, the forcing efficiencies are similar to those of the background aerosol. However, the changes in aerosol concentration due to the DD and BB inputs modulate the monthly averages of the radiative forcings at both BOA and TOA. In particular, the apportionment of these forcings between the 3 main aerosol components shows that the contribution of the BBM to RF_{BOA} and RF_{TOA} alike increases from 0 (in winter) to approximately 30% in October. The largest contribution of the DDM to RF_{BOA} and RF_{TOA} is obtained in April (53 and 66%, respectively) and it never falls below the 17 and 27% of the December month. This emphasizes again the importance of the desert dust component in Cairo's atmosphere.

Acknowledgments

This work has been partly funded by the French Ministry of Foreign Affairs in the frame of the Imhotep program (contract 446538E) and the Institut National des Sciences de l'Univers (INSU). The authors are grateful to Cairo University at Giza and the Egyptian Meteorological Authority (EMA), which have provided the two experimental sites, and to the PHOTONS/LOA and AERONET/NASA teams for calibrating the Sun photometer and processing its data.

References

Ackerman, A.S., Toon, Q.B., Stevens, D.E., Heymsfield, A.J., Ramanathan, V., Welton, E.J., 2000. Reduction of tropical cloudiness by soot. Science 288, 1042–1047.

Alfaro, S.C., Abdel Wahab, M., 2006. Extreme variability of aerosol optical properties: the Cairo aerosol characterization experiment case study. In: Perrin, A., et al. (Ed.), Remote Sensing of the Atmosphere for Environment Security. Springer Verlag, The Netherlands, pp. 285–299.

Alfaro, S.C., Lafon, S., Rajot, J.L., Formenti, P., Gaudichet, A., Maillé, M., 2004. Iron oxides and light absorption by pure desert dust: an experimental study. J. Geophys. Res. 109, D08208. doi:10.1029/2003JD004374.

Alpert, P., Kaufman, Y.J., Shay-El, Y., Tanre, D., da Silva, A., Schubert, S., Joseph, J.H., 1998. Quantification of dust-forced heating of the lower troposphere. Nature 395, 367–370.

Andreae, M.O., coauthors, 2002. Biogeochemical cycling of carbon, water, energy, trace gases, and aerosols in Amazonia: the LBA-EUSTACH experiments. J. Geophys. Res. 107 (D20), 8066. doi:10.1029/2001JD000524.

Andreae, M.O., Gelencser, A., 2006. Black carbon or brown carbon? The nature of light-absorbing carbonaceous aerosols, 2006. Atmos. Chem. Phys. 6, 3131–3148.
Ångström, A., 1964. The parameters of atmospheric turbidity. Tellus 14, 64–75.
Cerf, A., 1986. Atmospheric turbidity over West-Africa. Contrib. Atmos. Phys. 53, 414–429.
Charlson, R.J., Schwartz, S.E., Hales, J.M., Cess, R.D., Coakley Jr., J.A., Hansen, J. E., Hoffman, D.J., 1992. Climate forcing by anthropogenic aerosols. Science 255, 423–430. doi:10.1126/science.255.5043.423.
Che, H.Z., Zhang, X.Y., Alfaro, S., Chatenet, B., Gomes, L., Zhao, J.Q., 2009. Aerosol optical properties and its radiative forcing over Yulin, China in 2001 and 2002. Adv. Atmos. Sci. 26 (3), 564–576 10.1007/s00376-009-0564-4.
Chin, M., 2009. Atmospheric Aerosol Properties and Climate Impacts, U.S. Synthesis and Assessment Product 23, Reported by the U.S. Climate Science Program and the Subcommittee on Global Change Research. http://downloads.climatescience.gov/sap/sap2-3/sap2-3-final-report-all.pdf.
Derimian, Y., Karnieli, A., Kaufman, Y.J., Andreae, M.O., Andreae, T.W., Dubovik, O., Maenhaut, W., Koren, I., Holben, B.N., 2006. Dust and pollution aerosols over the Negev desert, Israel: properties, transport, and radiative effect. J. Geophys. Res. 111, D05205 10.1029/2005JD006549.
Dubovik, O., King, M.D., 2000. A flexible inversion algorithm for retrieval of aerosol optical properties from sun and sky radiance measurements. J. Geophys. Res. 105, 20,673–20,696.
Dubovik, O., Holben, B., Eck, T.F., Smirnov, A., Kaufman, Y.J., King, M.D., Tanre, D., Slutsker, I., 2002a. Variability of absorption and optical properties of key aerosol types observed in worldwide locations. J. Atmos. Sci. 59 (3), 590–608.
Dubovik, O., Holben, B.N., Lapyonok, T., Sinyuk, A., Mishchenko, M.I., Yang, P., Slutsker, I., 2002b. Non-spherical aerosol retrieval method employing light scattering by spheroids. Geophys. Res. Lett. 29 (10), 1415. doi:10.1029/2001GL014506.
Dubovik, O., Sinyuk, A., Lapyonok, T., Holben, B.N., Mishchenko, M., Yang, P., Eck, T.F., Volten, H., Muñoz, O., Veihelmann, B., van der Zande, W.J., Leon, J.F., Sorokin, M., Slutsker, I., 2006. Application of light scattering by spheroids for accounting for particle non-sphericity in remote sensing of desert dust. J. Geophys. Res. 111, D11208. doi:10.1029/2005JD006619.
Dubuisson, P., Buriez, J.C., Fouquart, Y., 1996. High spectral resolution solar radiative transfer in absorbing and scattering media, application to the satellite simulation. J. Quant. Spectros. Radiat. Transf. 55 (1), 103–126.
El-Askary, H., Kafatos, M., 2008. Dust storm and black cloud influence on aerosol optical properties over Cairo and the Greater Delta region, Egypt. Int. J. Remote Sens. 29 (24), 7199–7211.
El-Fandy, M.G., 1940. The formation of depressions of the Khamsin type. Q. J. R. Meteorol. Soc. 66, 323–335.
El-Fandy, M.G., El-Nisr, M.K., 1949. On the conditions favoring low stratus formation over the Middle East in summer. Bull. Am. Meteorol. Soc. 30, 357–359.
El-Metwally, M., Alfaro, S.C., Abdel Wahab, M., Chatenet, B., 2008. Aerosol characteristics over urban Cairo: seasonal variations as retrieved from Sun photometer measurements. J. Geophys. Res. 113, D14219. doi:10.1029/2008JD009834.
El-Wakil, S.A., El-Metwally, M., Gueymard, C., 2001. Atmospheric turbidity of urban and desertic areas of the Nile basin in the aftermath of Mt. Pinatubo's eruption. Theor. Appl. Climatol. 68, 89–108. doi:10.1007/s007040170056.
Favez, O., Cachier, H., Sciare, J., Alfaro, S., El-Araby, T.M., Harhash, M.A., Abdel wahab, M.M., 2008. Seasonality of major aerosol species and their transformations in Cairo megacity. Atmos. Environ. 42 (7), 1503–1516. doi:10.1016/j.atmosenv.2007.10.081.
García, O.E., García, O.E., Díaz, A.M., Expósito, F.J., Díaz, J.P., Dubovik, O., Dubuisson, P., Roger, J.-C., Eck, T.F., Sinyuk, A., Derimian, Y., Dutton, E.G., Schafer, J.S., Holben, B.N., García, C.A., 2008. Validation of AERONET estimates of atmospheric solar fluxes and aerosol radiative forcing by ground-based broadband measurements. J. Geophys. Res. 113, D21207. doi:10.1029/2008JD010211.
Hansen, J., couthors, 1997. Forcings and chaos in interannual to decadal climate change. J. Geophys. Res. 102, 25679–25720. doi:10.1029/97JD01495.
Haywood, J., Boucher, O., 2000. Estimates of the direct and indirect radiative forcing due to tropospheric aerosols: a review. Rev. Geophys. 38, 513–543.
Haywood, J.M., Shine, K.P., 1997. Multi-spectral calculations of the direct radiative forcing of the tropospheric sulphate and soot aerosols using a column model. Q. J. R. Meteorol. Soc. 123, 1907–1930.
Holben, B.N., Eck, T.F., Slutsker, I., Tanré, D., Buis, J.P., Setzer, A., Vermote, E., Reagan, J.A., Kaufman, Y.J., Nakajima, T., Lavenu, T., Jankowiak, I., Smirnov, A., 1998. AERONET—a federated instrument network and data archive for aerosol characterization. Remote Sens. Environ. 66, 1–16.
Intergovernmental Panel on Climate Change, 2007. The Physical Science Basis, Fourth Assessment Report Summary (2007). Cambridge Univ, Press, New York.
Junge, C.E., 1955. The size distribution and aging of natural aerosols as determined from electrical and optical data on the atmosphere. J. Meteorol. 12, 13–25.
Kaskaoutis, D.G., Kambezidis, H.D., Hatzianastassiou, N., Kosmopoulos, P.G., Badarinath, K.V.S., 2007. Aerosol climatology: on the discrimination of aerosol types over four AERONET sites. Atmos. Chem. Phys. Discussion 7, 6357–6411.
Kaufman, Y.J., Tanré, D., Gordon, H.R., Nakajima, T., Lenoble, J., Frouin, R., Grassl, H., Herman, B.M., King, M.D., Teillet, P.M., 1997. Passive remote sensing of tropospheric aerosol and atmospheric correction for the aerosol effect. J. Geophys. Res. 102 (D14), 16,815–16,830.
Kaufman, Y.J., Tanré, D., Dubovik, O., Karnieli, A., Remer, L.A., 2001. Absorption of sunlight by dust as inferred from satellite and ground-based remote sensing. Geophys. Res. Lett. 28 (8), 1479–1482.
Kaufman, Y.J., Tanré, D., Boucher, O., 2002. A satellite view of aerosols in the climate system. Nature 419, 215–223.
Kim, D.-H., Sohn, B.J., Nakajima, T., Takamura, T., 2005. Aerosol radiative forcing over east Asia determined from ground-based solar radiation measurements. J. Geophys. Res. 110, D10S22. doi:10.1029/2004JD004678.
King, M.D., Kaufman, Y.J., Menzel, W.P., Tanré, D., 1992. Remote sensing of cloud, aerosol, and water vapor properties from the Moderate Resolution Imaging Spectrometer (MODIS). IEEE Geosci. Remote Sens. 30, 2–27.
Lelieveld, J., coauthors, 2002. Global air pollution crossroads over the Mediterranean. Science 298, 794–799.
Liou, K.N., 2002. An Introduction to Atmospheric Radiation. Academic Press. 583pp.
Mahmoud, K.F., Alfaro, S.C., Favez, O., Abdel Wahab, M.M., Sciare, J., 2008. Origin of black carbon concentration peaks in Cairo (Egypt). Atmos. Res. 89, 161–169.
Mallet, M., Dingenen, R.V., Roger, J.C., Despiau, S., Cachier, H., 2005. In situ airborne measurements of aerosol optical properties during photochemical pollution events. J. Geophys. Res. 110, D03205. doi:10.1029/2004JD005139.
Mallet, M., Pont, V., Liousse, C., Roger, J.C., Dubuisson, P., 2006. Simulation of aerosol radiative properties with the ORISAM-RAD model during a pollution event (ESCOMPTE 2001). Atmos. Environ. 40, 7696–7705.
McFarlane, S.A., Kassianov, E.I., Barnard, J., Flynn, C., Ackerman, T.P., 2009. Surface shortwave aerosol radiative forcing during the Atmospheric Radiation Measurement Mobile Facility deployment in Niamey, Niger. J. Geophys. Res. 114, D00E06. doi:10.1029/2008JD010491.
Miller, R.L., Tegen, I., Perlwitz, J., 2004. Surface radiative forcing by soil dust aerosols and the hydrologic cycle. J. Geophys. Res. 109, D04203 doi:10.1029/2003JD004085.
Moorthy, K.K., Babu, S.S., Satheesh, S.K., 2005. Aerosol characteristics and radiative impacts over the Arabian Sea during the intermonsoon season: results from ARMEX field campaign. J. Atmos. Sci. 62, 192–206.
Nakajima, T., Sekiguchi, M., Takemura, T., Uno, I., Higurashi, A., Kim, D., Ju Sohn, B., Oh, S.-N., Nakajima, T.Y., Ohta, S., Okada, I., Takamura, T., Kawamoto, K., 2003. Significance of direct and indirect radiative forcings of aerosols in the East China Sea region. J. Geophys. Res. 108 (D23), 8658. doi:10.1029/2002JD003261.
Pandithurai, G.P., Devera, C.S., Raj, P.E., Sharma, S., 1997. Retrieval of aerosol size index from high-resolution spectroradiomter observations. Aerosp. Sci. Technol. 26, 154–162. doi:10.1080/02786829708965421.
Pandithurai, G., Dipu, S., Dani, K.K., Tiwari, S., Bisht, D.S., Devara, P.C.S., Pinker, R.T., 2008. Aerosol radiative forcing during dust events over New Delhi, India. J. Geophys. Res. 113, D13209. doi:10.1029/2008JD009804.
Pilewskie, P., 2007. Climate change: aerosols heat up. Nature 448, 541–542. doi:10.1038/448541a.
Ramanathan, V., Ramana, M.V., Roberts, G., Kim, D., Corrigan, C., Chung, C., Winker, D., 2007. Warming trends in Asia amplified by brown cloud solar absorption. Nature 448, 575–578. doi:10.1038/nature06019.
Remer, L.A., Kaufman, Y.J., Holben, B.N., Thompson, A.M., McNamara, D., 1998. Biomass burning aerosol size distribution and modeled optical properties. J. Geophys. Res. 103 (D24), 31,879–31,891. doi:10.1029/98JD00271.
Remer, L.A., Kaufman, Y.J., Holben, B.N., 1999. International variation of ambient aerosol characteristics on the east coast of the United States. J. Geophys. Res. 104, 2223–2231. doi:10.1029/1998JD200037.
Roger, J.C., Mallet, M., Dubuisson, P., Cachier, H., Vermote, E., Dubovik, O., Despiau, S., 2006. A synergetic approach for estimating the local direct aerosol forcing: application to an urban zone during the ESCOMPTE experiment. J. Geophys. Res. 111, D13208. doi:10.1029/2005JD006361.
Saha, A., Mallet, M., Roger, J.C., Dubuisson, P., Piazzola, J., Despiau, S., 2008. One year of measurements of aerosol optical properties over an urban coastal site: effect on local direct radiative forcing. Atmos. Res. 90, 195–202.
Scott, N.A., 1974. A direct method of computation of the transmission function of an inhomogeneous gaseous medium—I: description of the method. J. Quant. Spectros. Radiat. Transf. 14, 691–704.

Sokolik, I.N., Toon, O.B., 1999. Incorporation of mineralogical composition into models of the radiative properties of mineral aerosol from UV to IR wavelengths. J. Geophys. Res. 104, 9423–9444.

Tadros, M.T.Y., El-Metwally, M., Hamed, A.B., 2002. Determination of Ångström coefficients from spectral aerosol optical depth at two sites in Egypt. Renewable Energy 27, 621–645. doi:10.1016/S0960-1481(01)00156-2.

Tafuro, A.M., Kinne, S., De Tomasi, F., Perrone, M.R., 2007. Annual cycle of aerosol direct radiative effect over southeast Italy and sensitivity studies. J. Geophys. Res. 112, D20202. doi:10.1029/2006JD008265.

Tanré, D., Kaufman, Y.J., Holben, B.N., Chatenet, B., Karnieli, A., Lavenu, F., Blarel, L., Dubovik, O., Remer, L.A., Smirnov, A., 2001. Climatology of dust aerosol size distribution and optical properties derived from remotely sensed data in the solar spectrum. J. Geophys. Res. 106 (D16), 18,205–18,217.

Zakey, A.S., Abdel Wahab, M.M., Makar, P.A., 2004. Atmospheric turbidity over Egypt. Atmos. Environ. 38, 1579–1591.